



HAL
open science

Correlated Time-Varying Magnetic Fields and the Core Size of Mercury

Ingo Wardinski, Benoit Langlais, Erwan Thébault

► **To cite this version:**

Ingo Wardinski, Benoit Langlais, Erwan Thébault. Correlated Time-Varying Magnetic Fields and the Core Size of Mercury. *Journal of Geophysical Research. Planets*, 2019, 124 (8), pp.2178-2197. 10.1029/2018JE005835 . hal-02285506

HAL Id: hal-02285506

<https://hal.science/hal-02285506>

Submitted on 23 Nov 2020

HAL is a multi-disciplinary open access archive for the deposit and dissemination of scientific research documents, whether they are published or not. The documents may come from teaching and research institutions in France or abroad, or from public or private research centers.

L'archive ouverte pluridisciplinaire **HAL**, est destinée au dépôt et à la diffusion de documents scientifiques de niveau recherche, publiés ou non, émanant des établissements d'enseignement et de recherche français ou étrangers, des laboratoires publics ou privés.

Correlated time-varying magnetic fields and the core size of Mercury

I. Wardinski¹, B. Langlais¹ & E. Thébault¹

¹Laboratoire de Planétologie et Géodynamique, Université de Nantes, Université d'Angers, CNRS, UMR

6112, Nantes, France

Key Points:

- We model Mercury's magnetic field on a temporal basis with spherical harmonics
- We analyze time varying external (inducing) and internal (induced) magnetic fields
- We estimate Mercury's core size at 2060 ± 22 km

11 **Abstract**

12 Mercury is characterized by a very peculiar magnetic field, as it was revealed by the MES-
 13 SENDER mission. Its internal component is highly axisymmetric, dominated by the dipole,
 14 and very weak. This in turns leads to a very dynamic magnetosphere. It is known that
 15 there exist relationships between the internally generated field and the external field, al-
 16 though their dynamics are complex. In this study we derive steady and time-varying spher-
 17 ical harmonic models of Mercury’s magnetic field using MESSENGER measurements,
 18 and interpret these models both in terms of correlated features and of the internal struc-
 19 ture of Mercury. The influence of the hemispheric data distribution of MESSENGER
 20 is evaluated to grant the robustness of our models. We find a quadrupole-to-dipole ra-
 21 tio of 0.27 for the steady magnetic field. The time-varying models reveal periodic and
 22 highly correlated temporal variations of internal and external origins. This argues for
 23 externally inducing and internally induced sources. The main period is 88 days, the or-
 24 bital period of Mercury around the Sun. There is no measurable time lag between vari-
 25 ations of external and internal magnetic fields, which place an upper limit of 1 Sm^{-1} for
 26 the mantle conductivity. Finally, the compared amplitudes of external and internal time
 27 varying field lead to an independent (from gravity studies) estimate of the conductive
 28 core radius, at $2060 \pm 22 \text{ km}$. These analyses will be further completed with the upcom-
 29 ing BepiColombo mission and its magnetic field experiment, but the presented results
 30 already lift the veil on some of the magnetic oddities at Mercury.

31 **1 Introduction**

32 Since the beginning of its exploration with space-borne missions, it is known that
 33 Mercury has a magnetic field of internal origin (Ness et al., 1974a). This internal mag-
 34 netic field is relatively weak, $\sim 1\%$ of Earth’s magnetic field strength. It is character-
 35 ized by a strong axisymmetry and a large quadrupole-to-dipole ratio (Anderson et al.,
 36 2012; Johnson et al., 2012; Oliveira et al., 2015; Thébault et al., 2018). This internal field
 37 is significantly larger than the interplanetary magnetic field, and its interaction with the
 38 solar wind forms a bow shock wave and a magnetosphere (Ness et al., 1974b).

39 Several mechanisms have been proposed that could generate Mercury’s weak in-
 40 ternal magnetic field. These incorporate a thermo-electric dynamo process at a topograph-
 41 ically rough outer core surface (Stevenson, 1987), a dynamo driven by a thermo-compositional
 42 convection associated with the solidification of an inner core (Christensen, 2006), or a

dynamo process driven by convection that is affected by a radial gradient of the electrical conductivity at the outer core surface (Gómez-Pérez et al., 2010). Alternatively, Aharonson et al. (2004) suggested that the internal magnetic field could also be generated by the magnetization of Mercury’s crust and mantle due to an ancient (and perhaps extinct) dynamo process.

A number of studies highlighted the importance of the magnetospheric magnetic field, which may control the internal magnetic field generation of Mercury by a feedback mechanism (Glassmeier et al., 2007; Gómez-Pérez & Solomon, 2010; Heyner et al., 2011). The magnetosphere of Mercury results from an interaction of the solar wind and the planetary magnetic field. Its subsolar stand-off distance is $0.45 R_M$ above the surface of the planet, where $R_M = 2440$ km (Johnson et al., 2012; Winslow et al., 2013; Thébault et al., 2018). This interaction causes an electrical current to flow on the boundary of the magnetosphere across the tail of the magnetosphere, similar to the Chapman-Ferraro current system in Earth’s magnetosphere (Chapman & Ferraro, 1940, 1941).

Mercury’s orbital motion leads to periodic variations of the solar wind conditions that cause varying stand-off distances of the magnetosphere and variations of the magnetospheric magnetic field (Suess & Goldstein, 1979). One peculiarity of the Hermean system is related to the 3:2 resonance between the rotation of Mercury and its revolution around the Sun. It takes 3 rotations of the planet (58.65 days each), or 2 full orbits (87.67 days each), for Mercury to return to similar solar conditions, i.e. a given location sunlit under the same angle. The synodic period, i.e. the rotation of the Sun as seen from Mercury as it moves along its orbit, is close to 36 days.

As mentioned above, variations of the magnetospheric stand-off distance cause varying Chapman-Ferraro currents and generate a time-varying external magnetic field, which in turn induces a time-varying internal magnetic field in Mercury’s electrically highly conducting core (Hood & Schubert, 1979; Glassmeier, 2000; Grosser et al., 2004; Johnson et al., 2016). The induced magnetic field adds to the primary internal magnetic field. Several studies (Glassmeier, 2000; Grosser et al., 2004) estimated the induced magnetic field amplitude may reach about 10% of the mean internal magnetic field intensity at the planet’s surface. Closely related to magnetic field generation and the induction process is Mercury’s internal structure. Earth-based observations confirmed the presence of a metallic core, that contains a liquid part inside (Margot et al., 2007). The core of Mercury is

75 covered by a mantle, which may resemble Earth’s mantle in physical properties such as
76 composition and electrical conductivity (Rivoldini et al., 2009; Zhang & Pommier, 2017).
77 Geodetic observation of Mercury’s gravity field during the MESSENGER mission con-
78 fines the core radius to 2004 ± 39 km (Rivoldini & Van Hoolst, 2013); in combination
79 with Earth-based radar observations of the planet’s spin state the core size can be es-
80 timated as 2020 ± 30 km (Hauck et al., 2013). Note that these two results are estimates
81 of the liquid core radius. As pointed out by Hauck et al. (2013), the uppermost part of
82 the core could be solid and indistinguishable from the mantle. Johnson et al. (2016) found
83 Mercury’s core based on induction analyses at 1900-2200 km. The latter study highlighted
84 the potential of MESSENGER’s magnetic field measurements to infer the internal struc-
85 ture of Mercury. In this case, the radius estimate is that of the electrically conductive
86 core, regardless of its solid or liquid state.

87 The rapid dynamics of the solar wind, associated with the weak magnetic field of
88 Mercury and its orbital motion, lead to both fast magnetospheric changes and slow pe-
89 riodic variations. The aim of this study is thus to analyze and to compare the tempo-
90 ral variability of external and internal constituents of Mercury’s magnetic field. Anal-
91 yses are based on magnetic field measurements made by NASA’s MESSENGER mission
92 (Solomon et al., 2007). The paper is organized as follows. First we describe the used meth-
93 ods to isolate the static, or steady, constituents of the internal and external magnetic fields
94 of Mercury. We next derive residuals between the steady field model and magnetic field
95 measurements of MESSENGER, and we model them with a time-varying scheme in the
96 third section. Results are analyzed in the fourth section, where coherency between in-
97 ternal and external field variations is investigated. This allows to specify possible mech-
98 anisms that may generate and drive these magnetic field variations. One important out-
99 put is a new and non-geodetic estimate of the conductive core radius. We conclude our
100 study in the last section.

101 **2 Derivation of a steady magnetic field model**

102 **2.1 Data selection**

103 The MESSENGER spacecraft remained in orbit around Mercury from 18 March
104 2011 and lasted until 30 April 2015. During this period of 4 years, the spacecraft con-
105 tinuously measured Mercury’s magnetic field. The mission orbit was highly elliptical, with

106 a periapsis ranging from 200 to 500 km over the north polar region, and an apoapsis ex-
 107 ceeding 12700 km above the southern hemisphere at the beginning of the mission, low-
 108 ered to about 8000 km after one year. The altitude change also increased the number
 109 of orbits per day, from 2 to 3. This led to an uneven data distribution, and only mea-
 110 surements over the northern hemisphere are assumed to be inside the magnetospheric
 111 cavity which allow modeling of Mercury’s internal magnetic field. The entire planet is
 112 covered in 59 (terrestrial) days, and all local times are sampled twice within 176 days.
 113 MESSENGER returned magnetic field measurements in the MBF (Mercury Body Fixed)
 114 and in the MSO (Mercury Sun Oriented) reference systems. These are further described
 115 in Section 2.5.

116 Three different data selection schemes are considered, with the goal of deriving a
 117 steady magnetic field model. First, we select all data with a satellite altitude below 1000
 118 km. This scheme is denoted as `_alt`. Second, we select data using a proxy defined by Oliveira
 119 et al. (2015) that indicates whether the measurement are taken within the magnetospheric
 120 cavity or not. This is denoted as `_mag`. Third, data are selected during local night time
 121 and below 1000 km altitude (scheme `_a-n`). The selection of data only during local night
 122 times is often used in satellite based geomagnetic field modeling (e.g. Lesur et al., 2015;
 123 Finlay et al., 2016), and ensures reduced external magnetospheric field strengths (An-
 124 derson et al., 2013). The altitude selection criterion guarantees that the analyzed mag-
 125 netic field measurements are close enough to the surface of Mercury so that the inter-
 126 nal magnetic field dominates the signal. The altitude limit is below the average subso-
 127 lar distance of the magnetopause location (Winslow et al., 2013), which in turn should
 128 ensure the sampling of the magnetic field within a source-free region. The third data set
 129 is a subset of the second one, which is itself a subset of the first one.

130 2.2 Model description

131 In this study, the model of Mercury’s steady field is parameterised in terms of spher-
 132 ical harmonics, which is a widely used technique in geomagnetic field modeling (i.e. Lan-
 133 gel, 1987), and was applied earlier to derive models of planetary magnetic fields (i.e. Holme
 134 & Bloxham, 1996; Anderson et al., 2008; Uno et al., 2009). This is different to recently
 135 applied approaches to model Mercury’s magnetic field which sought to overcome the lack
 136 of magnetic field measurements in the southern hemisphere. For instance, Anderson et
 137 al. (2012) related magnetic equator crossings to the axisymmetric field. Oliveira et al.

138 (2015) used an equivalent source dipole scheme (Langlais et al., 2004) over the north-
 139 ern hemisphere only. Thébault et al. (2018) favored a parameterization based on local-
 140 ized functions over the northern hemisphere, using the revised spherical cap harmonic
 141 analysis method (Thébault et al., 2006).

142 However, as it has been shown by several studies (Ness et al., 1974a; Holme & Blox-
 143 ham, 1996; Uno et al., 2009; Ridley & Holme, 2016; Connerney et al., 2018) spherical
 144 harmonic analyses can provide robust estimates of planetary magnetic fields even from
 145 single fly-bys and un-even data distribution, provided some prior regularization. In a source-
 146 free region without electric currents, the steady magnetic potential is given by a spher-
 147 ical harmonic expansion

$$148 \quad V = a \sum_{l=1}^{L_{\text{int}}} \sum_{m=0}^l \left\{ (g_l^m \cos(m\phi) + h_l^m \sin(m\phi)) \left(\frac{a}{r}\right)^{l+1} P_l^m(\cos\theta) \right\} \quad (1)$$

$$149 \quad + a \sum_{l=1}^{L_{\text{ext}}} \sum_{m=0}^l \left\{ (q_l^m \cos(m\phi) + s_l^m \sin(m\phi)) \left(\frac{r}{a}\right)^l P_l^m(\cos\theta) \right\}, \quad (2)$$

150 where a is the Mercury’s mean radius (2440 km). r, θ, ϕ are the MBF planetocentric co-
 151 ordinates of MESSENGER, r the radial distance from the planetary center, θ the colat-
 152 itude, and ϕ the longitude. The $P_l^m(\cos\theta)$ are the Schmidt normalized associated Leg-
 153 endre functions, where l is the degree and m the order. L_{int} and L_{ext} are the truncation
 154 degrees of the spherical harmonic expansions for the internal and external field, respec-
 155 tively. The model parameters $\{g_l^m, h_l^m\}$ and $\{q_l^m, s_l^m\}$ are called Gauss coefficients and
 156 represent the internal and external magnetic field, respectively.

157 These model parameters are estimated by a least squares fit to data collected dur-
 158 ing a given time interval. For a linear inverse problem (least squares fit) the model vec-
 159 tor \mathbf{m} containing the Gauss coefficients is found at the minimum of an objective func-
 160 tion

$$161 \quad \Theta(\mathbf{m}) = (\mathbf{y} - \mathbf{A}\mathbf{m})^\top \mathbf{C}_e^{-1} (\mathbf{y} - \mathbf{A}\mathbf{m}) + \lambda_S (\mathbf{m}^\top \mathbf{C}_m \mathbf{m}), \quad (3)$$

162 where \mathbf{y} is the data vector, \mathbf{A} a design matrix, \mathbf{C}_e the data error covariance matrix, and
 163 \mathbf{C}_m the prior model covariance matrix (Jackson, 1979; Gubbins, 1983), controlled by a
 164 Lagrange multiplier, λ_S . The final model represents the optimal balance between data
 165 misfit and model smoothness, which is found for the λ_S at the knee of their trade-off curves.

166 The inverse problem is ill-posed, as a large number of observations have to be ex-
 167 plained by a truncated set of model parameters. This leads to an ambiguity in the in-
 168 version. In general, solving ill-posed inverse problems requires regularization to reduce

169 the ambiguity towards a prior constraint and to stabilize the solution of the inversion
 170 (Levenberg, 1944; Tarantola, 1987). A variety of spatial constraints could be applied to
 171 reduce the ambiguity of the inversion (see Holme and Bloxham (1996) for a discussion
 172 of spatial constraints). Here we choose to utilize a prior constraint that controls the com-
 173 plexity of the model field morphology at a chosen spherical surface of radius c . We em-
 174 ploy

$$175 \quad \mathbf{C}_m : \oint B_r^2 dS|_{r=c} = 4\pi \sum_{l=1}^{L_{\text{int}}} \sum_{m=0}^l \frac{(l+1)^2}{2l+1} \left(\frac{a}{c}\right)^{(2l+4)} (g_l^{m2} + h_l^{m2}) \quad (4)$$

176 to minimize the mean square radial field at Mercury’s surface, with $c = 2440$ km. The
 177 diagonal elements of \mathbf{C}_m are then

$$178 \quad \text{diag} \left[\frac{(l+1)^2}{2l+1} \left(\frac{a}{c}\right)^{(2l+4)} \right]. \quad (5)$$

179 As long as $a \geq c$, the diagonal elements of \mathbf{C}_m grow with the degree of spherical har-
 180 monics. Therefore, contributions of the higher degrees of spherical harmonics are more
 181 strongly regularized during the inversion, which ensures the convergence of the norm.

182 Usually, in geomagnetic field modeling c is set to the radius of Earth’s core. This
 183 could have been adopted here by using estimates of Mercury’s core radius, between $c =$
 184 2004 km and $c = 2030$ km (Rivoldini & Van Hoolst, 2013; Hauck et al., 2013). However,
 185 there are no reason why one value or the other should be chosen. In addition, the ra-
 186 dius of Mercury’s dynamo source region is not well known. We therefore set $c = a = 2440$
 187 km. This slightly modifies the effect of the prior constraint, as it regularizes terms of higher
 188 spherical harmonic degrees less strongly than when $c = 2004$ km or $c = 2030$ km, which
 189 may influence the resulting quadrupole-to-dipole ratio (a key parameter of Mercury’s mag-
 190 netic field).

191 **2.3 Maximum degree of the model, and separation of internal and ex-** 192 **ternal contributions**

193 The partial hemispherical coverage by the MESSENGER mission precludes large
 194 maximum degree in (1). This in turn may cause a spectral leakage, as the spectral en-
 195 ergy of unmodelled magnetic fields, i.e. $l > L$, are indefinitely mapped onto spherical
 196 harmonic degrees $l \leq L$. Possible sources could be magnetic fields of Mercury’s crust
 197 and core, but also its magnetosphere. In addition, a spectral leakage of external mag-
 198 netic field energy into the internal magnetic field model coefficients may also occur and
 199 vice versa (Thébault et al., 2012).

200 We perform a covariance analysis of the model inversion (see appendix A). Results
 201 (Fig. A.1) reveal significant correlations among coefficients across spherical harmonic de-
 202 grees. The clearest ones are for (g_1^0, g_2^0) , (g_1^1, g_2^1) , (h_1^1, h_2^1) , and (g_1^0, g_3^0) . Odd terms (l
 203 $= 1$ and $l = 3$) are correlated, and anti correlated to even terms ($l = 2$). Because of that,
 204 these coefficients can not be robustly and independently estimated. Their dependence
 205 can be directly related to the geometrical similarity of their spatial sensitivity, as well
 206 as to the uneven distribution of the MESSENGER data.

207 The covariance analysis of the model also shows that there is no significant spec-
 208 tral leakage between external and internal field coefficients (Fig. A.1). Those seem to
 209 be mostly independent of each other. We conclude that there is a good separation be-
 210 tween external and internal magnetic field sources.

211 We set the maximum spherical harmonic degree of the internal field L_{int} to 3 in
 212 (1). This choice is made because we seek to model only the large scale and internal mag-
 213 netic field. A choice with $L_{\text{int}} = 1$ could also have been considered. However, then the
 214 model would not have allowed to derive the quadrupole-to-dipole ratio of Mercury's mag-
 215 netic field, a key parameter.

216 Concerning the external field, derivation and interpretation of models with $L_{\text{ext}} >$
 217 1 are uncertain, because the convergence of (4) is not guaranteed, as the norm (4) is not
 218 bounded anymore ($c > a$), and therefore with no control on small scale external field
 219 contributions. The external field estimation of even vs. odd spherical harmonic degrees
 220 is also subject to the uneven spatial distribution of MESSENGER data. To this end, we
 221 set the maximum spherical harmonic degree of the external field L_{ext} to 1, without us-
 222 ing any prior constraint.

223 2.4 Inversion results

224 We present in Tab. 1 the number of selected measurements for each selection scheme,
 225 and the misfit of the associated models. Table 2 lists the coefficients of the different steady
 226 field models in the MBF coordinate system and also reports those of Anderson et al. (2012)
 227 and Thébault et al. (2018).

228 The best fit to the measurements is found for model `_a-n`. This is mainly because
 229 this selection scheme rejects day side measurements, limiting the effect of the external

230 field which is widely reduced during night local times. The other data selection schemes,
 231 i.e. `_alt` and `_mag`, do not suspend local day time data from the model derivation, ex-
 232 plaining their larger associated misfits. When compared to previously published mod-
 233 els, the best agreement is found between the global internal field description of Thébaud
 234 et al. (2018) and the model based on data selection scheme `_a-n`. The external field co-
 235 efficients; however differ and indicate that the night side external field is on average less
 236 intense. Differences between models `_alt`, `_mag` and that of Thébaud et al. (2018) can
 237 be explained by similar reasons: they are likely due to magnetic fields generated by elec-
 238 trical currents flowing at day times in the plasma environment of Mercury, that are not
 239 excluded by the data selection. We finally note that models `_alt` and `_mag` have similar
 240 internal field coefficients as the model by Anderson et al. (2012) which is based on the
 241 first 9 months of measurements, and for which data include all local times.

242 Our preferred Model is model `_a-n`, as it provides the best estimate of Mercury’s
 243 large scale steady internal field. By using estimates of the covariance matrix we can also
 244 compute a formal error associated with the Gauss coefficients (Bloxham et al., 1989).
 245 This error or uncertainty is found to be $\sim 6\%$ for each coefficient.

246 2.5 Maps of the residual fields

247 Before the temporal variability of the residual magnetic field is studied in detail,
 248 we describe the spatial characteristics of the residual field. Residuals, $\delta\mathbf{B}$, between MES-
 249 SENDER measurements and the steady field model, \mathbf{B}_M , are computed using model `_a-`
 250 `n`,

$$251 \quad \delta\mathbf{B} = \mathbf{B} - \mathbf{B}_M. \quad (6)$$

252 These residuals are computed in both the MBF and MSO reference frames. The con-
 253 version from the MBF residual components $(\delta B_r, \delta B_\theta, \delta B_\phi)$ to the MSO ones $(\delta B_x, \delta B_y,$
 254 $\delta B_z)$, with x pointing towards the Sun, follows:

$$255 \quad \begin{aligned} \delta B_x &= \delta B_r \sin \theta_S \cos \phi_S + \delta B_\theta \cos \theta_S \cos \phi_S - \delta B_\phi \sin \phi_S, \\ 256 \quad \delta B_y &= \delta B_r \sin \theta_S \sin \phi_S + \delta B_\theta \cos \theta_S \sin \phi_S + \delta B_\phi \cos \phi_S, \\ 257 \quad \delta B_z &= \delta B_r \cos \theta_S - \delta B_\theta \sin \theta_S. \end{aligned} \quad (7)$$

258 ϕ_S and θ_S are solar longitude and latitude.

259 Residuals in the MBF system for ascending (pole ward) orbital legs during one Her-
 260 mean year (88 terrestrial days between two consecutive perihelions of Mercury) are shown
 261 in Fig. 1. Those in the MSO system for the same time-span are also displayed in the same
 262 figure (bottom panel). The maps in the MBF coordinate system do not show a simple
 263 residual field morphology. The considered time period corresponds to 1.5 full tour of MES-
 264 SENDER around Mercury. The western hemisphere (negative longitude) is covered twice.
 265 The overlapping field residuals are actually very different, with negative and positive fea-
 266 tures sensed over the same location but at different epochs. This strongly suggests that
 267 these residuals cannot be associated with steady internal sources. This conclusion was
 268 also reached by Johnson et al. (2012); Korth et al. (2015). When these residuals are plot-
 269 ted in the MSO reference frame, they show a different organization. The δB_x residuals
 270 show moderate to large positive amplitudes and arrange in a circular pattern centered
 271 in the North pole with an approximate latitudinal range from 60 to 87 degrees. The δB_y
 272 residuals (same Figure, middle panel) show a noticeable and regular pattern of positive
 273 and negative amplitudes centered around the North pole. This may suggest a substan-
 274 tial unmodelled small scale contribution of axial symmetry, i.e. possibly of degree 4 and
 275 order 2. In the midday to dusk section (longitudes from 0 to -90°) and in the midnight
 276 to dawn section (longitudes from 180 to 90°) significant residuals exist in a latitudinal
 277 band close to the equator. The map of δB_z (right panel) shows a region with large pos-
 278 itive residuals at the day-side. This region starts slightly after sunrise and extends some-
 279 what into the night-section. Near the North pole two small areas with opposite polar-
 280 ity are found, and may be related to processes in the polar cusp, and possibly linked to
 281 Birkeland currents, which are signatures of a magnetospheric circulation (Slavin et al.,
 282 1997; Anderson et al., 2014). These large scale residual patterns are also found in most
 283 other epochs of the mission’s lifetime, with positions fixed with respect to the Sun.

284 **3 Model of the time-varying residual fields**

285 We now turn to the modeling of these unmodelled magneticfield by subtracting the
 286 steady field MBF_a-n model from MESSENGER’s magnetic field measurements below
 287 1000 km altitude by using (6). Here, we do not discard measurements on the day side,
 288 nor do we use the criterion defined by Oliveira et al. (2015). The set of residual data is
 289 also fitted by spherical harmonic expansions, i.e. (1). As discussed in section 2.3 the deriva-

290 tion of external field models with of $L_{\text{ext}} > 1$ is omitted. For the internal field, we set
 291 L_{int} to 3. This choice is consistent with the approach taken for the steady fields.

292 Instead of inverting the entire data set at once, it is sorted in sub-samples of a given
 293 length as defined below. This approach allows to derive time series of internal and ex-
 294 ternal Gauss coefficients. The length or duration of each sub samples is defined using
 295 the following requirements: (1-a) have an optimal temporal resolution; (1-b) have a good
 296 spatial coverage. These are needed to construct (2-a) robust estimates of spatially large
 297 scale external and internal field contributions, leading to (2-b) characterize significant
 298 temporal magnetic field variations. With these objectives, we tested different temporal
 299 sampling and grouping of the data to invert them in terms of time series of Gauss co-
 300 efficients. Different settings of the data sampling are examined, some for which the data
 301 are sorted into overlapping or non-overlapping segments of 2 to 20 days length (tempo-
 302 ral sub-sampling). We also tested an orbital sub-sampling, where the data set is sorted
 303 to keep a constant number of consecutive orbits. Generally, it is found that data sets cov-
 304 ering longer time intervals show weaker temporal variability of the derived individual Gauss
 305 coefficients, likely because variations cancel out over longer time span. Orbital sub-sampling
 306 leads to an uneven temporal resolution, with Gauss coefficients derived every 2.5 to 5
 307 days, depending on the number of orbits per day or on possible data gaps, while provid-
 308 ing a more even spatial sampling than the temporal sub-sampling. For the latter rea-
 309 son we prefer orbital sub-sampling of the residual data set, and find that non-overlapping
 310 sets of 8 orbits provide reasonable inversion results. Figure 2 shows the residual field com-
 311 ponents after the further subtraction of time varying fields in MBF and MSO coordinate
 312 systems for the same time period as in Figure 1. Amplitudes of the remaining field are
 313 significantly reduced. The rms misfit of all 8-orbits samples ranges between 4 nT and
 314 30 nT, and its average is approximately 16 nT. Remaining structures are caused by un-
 315 modelled fields with, perhaps, different sources.

316 In the following we analyze coefficients of the first spherical harmonic degree only.
 317 Coefficient time series of the varying field consist of $\delta g_1^0(t)$, $\delta g_1^1(t)$, $\delta h_1^1(t)$ for the inter-
 318 nal field and $\delta q_1^0(t)$, $\delta q_1^1(t)$, $\delta s_1^1(t)$ for the external field. Their formal error ranges between
 319 9 and 12% for the internal coefficients, while those of the external field tend to be some-
 320 what smaller.

321 To allow for a time series analysis (Section 4) we interpolate series of Gauss coef-
 322 ficients with a spline function (de Boor, 1978), and compute a regular temporal division
 323 of one day. We note that the resulting temporal resolution of the time series remains close
 324 to 5 days.

325 3.1 Inversion results for the time-varying coefficients

326 Fig. 3 shows time series of the 6 Gauss coefficients of Mercury’s time varying in-
 327 ternal and external magnetic fields computed from residuals in the MBF coordinate sys-
 328 tem. The series of axial components, δg_1^0 and δq_1^0 (shown in the top panel of Fig. 3) seem
 329 to oscillate with a common period and show a fixed phase relation. Both coefficients show
 330 also a long term variability. It is clearly seen as an amplitude variation with smaller am-
 331 plitudes between 2013.0 and 2013.5, and larger amplitudes at the beginning and end of
 332 the mission. There is an apparent absolute shift between the axial coefficients, the in-
 333 ternal one being most of the time about 20 nT larger than the external one. The inter-
 334 nal equatorial terms (bottom panel, Figure 3), δg_1^1 and δh_1^1 , show similar amplitudes, which
 335 vary over time and with slightly larger amplitudes around 2013.0 - 2013.5. Their am-
 336 plitudes are smaller than those of the external equatorial terms δq_1^1 and δs_1^1 . Further-
 337 more, the variation of equatorial external and internal terms show more complex phase
 338 relations.

339 The cause for the long-term variation of δg_1^0 and δq_1^0 could be related to the vary-
 340 ing geometry of MESSENGER’s orbit over the mission period. Around 2013.2 the peri-
 341 apsis of MESSENGER reached its northernmost latitude. At this epoch the data dis-
 342 tribution was more or less symmetric on the ascending and descending legs of the orbits,
 343 i.e., with a similar number of measurements on the day and night sides. Before and af-
 344 ter this epoch, individual orbital legs were dominated by the descending and ascending
 345 part, respectively. In other words, there were more data on one or the other side of the
 346 planet, either day or night depending on the epoch. We investigated the effect of the sym-
 347 metric or not-symmetric data distribution on the resulting coefficients and performed
 348 a covariance analysis (see appendix A). Although the covariance matrix varies with time,
 349 there is no clear relationship with the varying periapsis latitude.

3.2 Magnetic dipole moments

In order to compare the internal and external magnetic field contributions, we compute their mean surface value, similarly to the approach of Grosser et al. (2004). For the internal field, it is

$$M_{\text{int}} = \sqrt{(l+1) \sum_{l=1}^{L_{\text{int,max}}} \sum_{m=0}^{m=l} [(g_l^m)^2 + (h_l^m)^2]}. \quad (8)$$

For the dipole, $L_{\text{int,max}} = 1$, this quantity becomes the dipole moment and is expressed as

$$M_{\text{int}}(t) = \sqrt{2 * ((g_1^0 + \delta g_1^0)^2 + (g_1^1 + \delta g_1^1)^2 + (h_1^1 + \delta h_1^1)^2)}. \quad (9)$$

The dipole moment of the static or time-averaged internal field is

$$\overline{M}_{\text{int}} = \sqrt{2 * ((g_1^0)^2 + (g_1^1)^2 + (h_1^1)^2)}. \quad (10)$$

The time-varying internal dipole moment is finally defined by

$$\delta M_{\text{int}}(t) = M_{\text{int}}(t) - \overline{M}_{\text{int}}. \quad (11)$$

For the dipole moment of the external field the expression is

$$M_{\text{ext}}(t) = \sqrt{l \sum_{l=1}^1 \sum_{m=0}^{m=l} [(q_l^m)^2 + (s_l^m)^2]}, \quad (12)$$

Our definition of dipole moments is in accordance with the field energy (Mauersberger, 1956; Lowes, 1966) and differs from the definition given by Grosser et al. (2004), who used the factor $(l+1)$ in (12). While these dipole moments are dominated by axial terms, they also take into account the equatorial ones, and as such, are more complete proxies of the large scale internal and external field temporal variations at Mercury.

Figure 5 shows series of the external and internal magnetic dipole moments at the planet surface. The variation of both is similar and apparently in phase. The amplitude of $M_{\text{ext}}(t)$ ranges from 20 to 120 nT, and the amplitude of $\delta M_{\text{int}}(t)$ is between ± 70 nT. These values have to be compared to $\overline{M}_{\text{int}}$, which we estimated at 305 nT for the dipole.

4 Results

4.1 Comparison with Mercury's orbit evolution

We now compare the temporal variability of the external magnetic dipole moment with the position of Mercury around the Sun, i.e. its heliocentric distance, in Fig. 6. The

377 external field varies with the heliocentric distance, but does not show a constant phase
 378 relation with the heliocentric distance. Prior to 2013.0 variation of the heliocentric dis-
 379 tance runs ahead variations of $M_{\text{ext}}(t)$. Maxima of $M_{\text{ext}}(t)$ occur slightly before Mer-
 380 cury’s perihelion. After 2014.0, maxima occur shortly later than the perihelion. We in-
 381 terpret this phase change to be related to the evolution of MESSENGER’s orbital ge-
 382 ometry.

383 The plots in the bottom part of Fig. 6 show MESSENGER’s orbits for selected epochs
 384 in the MSO reference frame. For the epoch 2011.49 a minimal external field is observed
 385 when MESSENGER had its lowest measurement point on the night side. We find a max-
 386 imum of the external field at 2011.64, when MESSENGER’s periapsis is at day. How-
 387 ever, the latitude of the MESSENGER’s periapsis is not constant with Mercury’s rota-
 388 tion period (59 days). The same latitude of the periapsis and the same local time is reached
 389 approximately every 54 days. It is suspected that such a latitudinal difference could trans-
 390 late into a temporal shift due to a hemispherical magnetic asymmetry. For instance, mag-
 391 netic field patterns that may only exist in a confined latitudinal range. A periapsis of
 392 MESSENGER over this region would occur on different local times, for which the strength
 393 of these magnetic fields may be different. When MESSENGER had its periapsis close
 394 to the north pole, the lowermost measurements were close to dawn and dusk. This may
 395 explain why the minimum and maximum external fields are less intense.

396 4.2 Results of the spectral analysis

397 We now turn to the spectral analysis of Mercury’s external and internal field vari-
 398 ability (details of the method are provided in appendix B). Figure 7 shows power spec-
 399 tra of the dipole Gauss coefficients representing the large scale of Mercury’s internal and
 400 external time-varying magnetic fields. Several spectral peaks can be identified. We mark
 401 6 different significant periods in the individual spectra with colored bars. These periods
 402 are related to Mercury’s orbital period of 88 days (annual period) and its first two sub-
 403 harmonics at 44 and 29 days, the rotation period of 59 days, and Mercury’s length of
 404 solar day of 176 days, respectively. The synodic rotation of the Sun as seen from Mer-
 405 cury, at 36 days, also shows a peak.

406 Peaks show different spectral strengths depending on the coefficients. For instance
 407 the synodic period (orange bar) is significant in the equatorial coefficients of the inter-

408 nal and external field but not in the axial ones. Signals related to the orbital period (44
 409 and 88 days) are significant in the axial field components and faintly appear in the equa-
 410 torial terms. These spectral peaks show a prominent doublet structure. The 176-days
 411 period causes a noticeable peak in all spectra, but significant peaks are found only for
 412 the equatorial terms of external and internal fields. These peaks tend to be slightly broader,
 413 which may reflect a slightly poorer sensitivity of the spectral estimation towards long-
 414 term cycles that are only a few times accommodated in the time series.

415 Spectra of the varying internal and external dipole moments $\delta M_{\text{int}}(t)$ and $M_{\text{ext}}(t)$
 416 are shown in Figure 8. Distinct spectral peaks can be identified and we mark the same
 417 periods in the individual spectra with colored bars as in Figure 7. Significant peaks are
 418 related to Mercury’s orbital period and its harmonics at 44 and 29 days (dark magenta
 419 bars), whereas other periods show no significant peaks. These peaks show, again, a dou-
 420 ble structure. We interpret this as being caused by the slight phase change that occurred
 421 around the middle epoch of the mission, when MESSENGER reached its most north-
 422 ern periapsis around 2013.2. This is further confirmed when performing spectral ana-
 423 lyzes separately before and after 2013.2, then peaks associated with the orbital period
 424 and its harmonics appear as single peaks.

425 **4.3 Results of the coherence analysis**

426 Significant periods which are identified in both dipole moments series may provide
 427 an appropriate measure to diagnose mutual coherent behavior using methods of coher-
 428 ence analysis (see appendix B for details). Figure 9 shows coherence and phase spectra
 429 of the two time series $\delta M_{\text{int}}(t)$ and $M_{\text{ext}}(t)$. The coherence spectrum is very detailed and
 430 shows numerous significant spectral peaks, which mostly relate to the spectral bands ob-
 431 served in the individual series (Figure 8). The annual variation (88 days) is significant
 432 in individual spectra of the magnetic dipole moments, and so is its MTM-coherence. The
 433 semi-annual variation (44 days) is found in the internal and external dipole moment vari-
 434 ations, but it causes no notable peak in the coherence, unlike the 29-day period.

435 There are also coherent peaks which do not exist in the spectra of the individual
 436 series. Most prominent are 5 such peaks in a period range between 88 and 176 days. Pos-
 437 sibly, these peaks are caused by superposition or combination of different periods. For
 438 instance, a superposition of the annual and the semi-annual period could lead to a vir-

439 tual period of 132-days, which is observed. It is found that these combinations involve
 440 all periods identified in Figure 8, even though they are not significant in the individual
 441 spectra of the dipole moments.

442 The phase spectrum is shown in Figure 9 (bottom panel). Non-zero phase angles
 443 indicate a leading or a trailing of $M_{\text{ext}}(t)$ with respect to $\delta M_{\text{int}}(t)$, if the angle is pos-
 444 itive or negative. The phase angle refers also to a lag-time, which depends on the given
 445 coherent period. The light-colored region in the phase spectrum displays the area of phase
 446 uncertainty of the 0 degree phase angle. This area is determined by the sub-sampling
 447 of the residual data into 8-orbits sample and by the applied spline interpolation in sec-
 448 tion 3. A phase angle within this area is not resolved by our analysis. None of the sig-
 449 nificant coherent periods show angles which are outside light-colored region. This means
 450 that lag-times can not be clearly resolved by the analysis. We therefore interpret the phase
 451 angles of all coherent periods to be indistinguishable from zero, and that lag-times are
 452 shorter than 5 days for these coherent periods. Variations in $\delta M_{\text{int}}(t)$ and $M_{\text{ext}}(t)$ can
 453 be assumed to be coincident.

454 Finally, Figure 10 shows the wavelet coherence between $\delta M_{\text{int}}(t)$ and $M_{\text{ext}}(t)$ se-
 455 ries. Significant coherence is mainly observed in a period range from 70 to 140 days, with
 456 a center at the 88-days period. The widening of this band is likely caused by the super-
 457 position of the 88-days period with other periods, as discussed for the results. Further
 458 coherence patches are also found for shorter periods, but they appear to be discontin-
 459 uous in time.

460 Most noticeable is the gap between patches of significant coherence in the middle
 461 of observation period around day 720, i.e. around 2013.2. The extent of this gap is roughly
 462 100 days, but may vary depending on the significance level applied for the wavelet co-
 463 herence.

464 From the coherence analyses we conclude that MTM-coherence and wavelet-coherence
 465 reveal coherent temporal variability of the internal and external dipole moments. Sig-
 466 nificant coherence exists in an approximate period range from 60 to 150 days. This con-
 467 firms the coherent temporal behavior related to the 88-days period, i.e., the period of
 468 Mercury’s motion around the Sun. Other periods show no clear coherence. Coherent vari-
 469 ations show no phase angles and appear to be simultaneous.

5 Discussion and implications

Results of this study may hold implications for our understanding of different magnetic field generation processes that are sampled by MESSENGER’s magnetometer data. In the following, we discuss results of the steady magnetic field modeling and the residual field analysis.

5.1 The steady magnetic field

Perhaps, one important result that can be derived from our steady field model is the quadrupole-to-dipole ratio. We find $g_2^0/g_1^0 = 0.27$, which is in agreement with the value reported by Thébault et al. (2018), but use a different modeling method. The reason why our value of the g_2^0/g_1^0 ratio and that of Thébault et al. (2018) largely differ from the value of Anderson et al. (2012) may be explained by several reasons. One is related to the data selection. Anderson et al. (2012) considers data from all local times in the model derivation, whereas this study uses only local night time data below 1000 km altitude to derive the internal magnetic field model. The selection of night time data reduces contributions from external fields, which have a significant impact on internal field coefficients. This can clearly be seen in Table 2, where we compare models derived from all local times and night time data. However, we note that Thébault et al. (2018) did not specifically reject day side measurements, so this is not the only explanation. The far-field modeling technique, as applied by Anderson et al. (2012) to derive their magnetic field model might be prone to current systems in Mercury’s magnetosphere and their related magnetic fields. This approach may also favor a high quadrupole-to-dipole ratio as it emphasizes equatorial data and down-weight data over polar regions (Thébault et al., 2018). We note that Anderson et al. (2008) obtained a lower quadrupole-to-dipole ratio which is comparable to ours, when the magnetospheric magnetic field is accounted by using an empirical model of the magnetopause and tail currents similar to that of Tsyganenko and Sitnov (2005). Therefore the true quadrupole-to-dipole ratio may still be a matter of debate, as the non-uniqueness imposed by MESSENGER’s data distribution critically hampers the determination of the spherical harmonics even degree terms, and therefore affects g_2^0/g_1^0 ratio.

We additionally derive the ratio of dipole to non-dipole axial terms by

$$D = \frac{|g_1^0|}{\sqrt{(g_2^0)^2 + (g_3^0)^2}}. \quad (13)$$

501 The ratio provides a simplified measure of the magnetic field dipolarity (Christensen et
 502 al., 2010). It is $D = 3.2$ for the model MBF_a-n and it deviates from the value derived
 503 from the coefficients given by Anderson et al. (2012), that is $D = 2.5$. Earth’s value
 504 derived from the IGRF (International geomagnetic reference field Thébaud et al., 2015)
 505 at epoch 2015 is $D = 6.2$. This value is computed at the same relative distance from
 506 the liquid core, as for Mercury. The values for Mercury largely differ from Earth’s value,
 507 indicating that Mercury’s magnetic field is less dipolar than Earth’s magnetic field. The
 508 so-called dipole offset is, therefore, a characteristic feature of Mercury’s low magnetic
 509 field dipolarity. Values of the dipolarity based on model by Anderson et al. (2012) and
 510 those derived from this study differ.

511 **5.2 Time-varying magnetic fields**

512 The relevance of our results of the time-varying modeling relies on the correctness
 513 of our assumption that measurements are acquired in a magnetic source-free region. This
 514 is likely to be the case, as the altitude range below 1000 km is negligibly populated by
 515 Ions. Only Birkeland currents are expected to exist at low altitudes in a confined cone
 516 of $15^\circ - 30^\circ$ in colatitude around the North pole (Anderson et al., 2014).

517 In our spectral analyses of the external and internal dipole moment variation that
 518 are mostly determined by the variation of δg_1^0 and δq_1^0 (see (11)), we identify 3 spectral
 519 peaks, which are related to the 88-days orbital period of Mercury, i.e., the annual pe-
 520 riodicity and its sub-harmonics. The identified 29-days period is indeed the second sub-
 521 harmonic of Mercury’s orbital period, as well as it could be the first sub-harmonic of the
 522 Mercury’s rotation period at 59 days. However, this period is not found in the spectral
 523 analyzes and therefore should not show sub-harmonics. These lead to the conclusion that
 524 the temporal variability of the internal and external residual fields is tightly linked to
 525 Mercury’s orbital motion around the Sun.

526 Similar conclusions have been reached by previous studies (Suess & Goldstein, 1979;
 527 Winslow et al., 2013; Johnson et al., 2016; Korth et al., 2017), where external field vari-
 528 ations are found to be related to the magnetopause stand-off distance. It varies with the
 529 planet’s heliocentric distance and the changing solar wind pressure during the planet’s
 530 orbit generates a varying external magnetic field around Mercury. The doublet peaks
 531 of annual and semi-annual variations in the spectra of the axial dipole coefficients and

532 the dipole moments (Figs. 7 and 8) disappear when the analysis is ran separately for pe-
 533 riods prior or after 2013.2. Therefore, the split-up is possibly related to the phase shift
 534 seen in Figure 6 which is a consequence of the changed orbital geometry of MESSEN-
 535 GER. External field variations seem to be fixed with respect to the Sun and do not co-
 536 rotate with Mercury, as we find no significant signals related to the 59-days period (side-
 537 real rotation period).

538 Another feature is the low variability of the axial terms and dipole moments around
 539 2013.2, see Figure 3. The wavelet coherence of $\delta M_{\text{int}}(t)$ and $M_{\text{ext}}(t)$ in Figure 10 dis-
 540 plays a distinct gap centered around 2013.2, which can be related to MESSENGER’s most
 541 northern periapsis.

542 **5.3 Electrical conductivity of the mantle**

543 Overall, the synchronous behavior of external and internal field variations at co-
 544 herent periods suggests a possible interpretation that involves the induction of internal
 545 magnetic fields due to external magnetic field variations. Such effect has been studied
 546 previously (Grosser et al., 2004; Heyner et al., 2016; Johnson et al., 2016).

547 If we assume the variation of the internal magnetic dipole moment to be dominantly
 548 caused by an induction process in the core driven by external field variations, then im-
 549 plications for the electrical mantle conductivity can be derived. Following Suess and Gold-
 550 stein (1979), the characteristic time for the external field to diffuse through Mercury’s
 551 mantle to the core is given by:

$$552 \quad \tau_D \approx \mu_0 \sigma_M L^2, \quad (14)$$

553 where μ_0 is the permeability of free space, σ_M the electrical mantle conductivity and L
 554 = 440 km the mantle thickness, respectively. This characteristic time corresponds to the
 555 delay that would be observed between the inducing external field and its induced inter-
 556 nal counterpart.

557 By using (14), we can derive an upper limit of the electrical mantle conductivity.
 558 All reported temporal variations are highly correlated and associated with a time-lag which,
 559 if it exists, is below our sensitivity of 5 days. This corresponds to an upper limit of \sim
 560 1 S/m. Shorter time-lags, yet unresolved by our approach, would correspond to smaller
 561 values of the electrical mantle conductivity. The electrical conductivity of Earth-like ma-
 562 terials like olivine and magnetite ranges from 10^{-4} S/m to 10^3 S/m at 300 K (Parkin-

563 son & Hutton, 1989). Our result agrees with synthetic electrical conductivity profiles of
 564 Mercury’s mantle and crust which range from 10^{-4} S/m to 1 S/m for different scenar-
 565 ios of Mercury’s formation by Verhoeven et al. (2009).

566 **5.4 Mercury’s core size**

567 We now attempt to derive the Mercury’s core size and adopt a formalism that was
 568 derived by Grosser et al. (2004), which expands the study of Rikitake (1966). Their study
 569 showed, that for an exciting external magnetic field variation, B_{exc} , with periods of the
 570 order of 1 second and longer, the ratio of internally induced (B_{ind}) to the exciting ex-
 571 ternal magnetic fields can be approximated by:

$$572 \quad \frac{B_{\text{ind}}}{B_{\text{exc}}} = \frac{n}{n+1} \left(\frac{r_c}{a} \right)^{2n+1}. \quad (15)$$

573 Our results show that external and internal magnetic fields are correlated with a period
 574 close to 88 days (Figs. 7, 8, 9 and 10). Such a relationship can also be represented by
 575 Gauss coefficients (Olsen, 1999; Tarits & Grammatica, 2000), particularly when the ex-
 576 ternal and internal fields can be largely described by a single coefficient, like axial dipole
 577 terms. But this fails for Mercury, where equatorial terms cannot be ignored. It is, there-
 578 fore, necessary to use magnetic dipole moments ((8) to (12)). However, one has also to
 579 take into account the internal magnetic field moment related to dynamo processes (10),
 580 and to consider instead the time-varying one (11). This poses a further complication,
 581 as the external dipole moment $M_{\text{ext}}(t)$ is always positive, while the internal $\delta M_{\text{int}}(t)$ has
 582 both positive and negative values, with a close-to-zero average. For these reasons we con-
 583 sider B_{exc} and B_{ind} in (15) to be equivalent with $M_{\text{ext}}(t)$ and $\delta M_{\text{int}}(t)$ only for epochs
 584 when those two terms are positive, i.e., for 259 epochs (out of 507). The arithmetic mean
 585 values are found to be 19.8 and 65.7 nT for internal and external parts, respectively.

586 Rearranging (15), and introducing the mean time-varying internal and external dipole
 587 moments, i.e., $n = 1$, we find Mercury’s core radius to be

$$588 \quad r_c = a \left(\frac{n+1}{n} \frac{B_{\text{ind}}}{B_{\text{ext}}} \right)^{1/(2n+1)} = a \left(2 \frac{|\delta M_{\text{int}}(t)|}{|M_{\text{ext}}(t)|} \right)^{1/3} = 2060 \text{ km}. \quad (16)$$

589 This value has to be seen as that of the electrically conductive core of Mercury, i.e., not
 590 necessarily that of the dynamo nor of its liquid part. In order to derive an error bar, we
 591 use the uncertainty estimates of the inversion, which yields an average formal error of
 592 10% for each coefficients. This is slightly more than for the static, mean field model, as

593 the static model is based on a much larger data set. Assuming the magnetic field coef-
 594 ficients to be Gauss-distributed random variables, the uncertainty range of dipole mo-
 595 ments is $\sim 17.3\%$. The uncertainty of the core radius estimates, which is based on 259
 596 samples, becomes $0.173/\sqrt{258} = 1.1\%$. This is approximately ± 22 km.

597 Our result (2060 ± 22 km) is consistent with the result of Johnson et al. (2016) who
 598 gave a conductive core radius range of [1900-2060 km] or [2020-2200 km], depending on
 599 the external field magnetic field model. Although it is also independent from geodetic
 600 observations, it is consistent with results of Rivoldini and Van Hoolst (2013) and Hauck
 601 et al. (2013), who found values of 2004 ± 39 km and 2020 ± 30 km for the liquid core
 602 radius, respectively.

603 **6 Conclusion**

604 In this study, we derive robust models of the steady external and internal magnetic
 605 fields of Mercury, based on a spherical harmonic analysis. External and internal mag-
 606 netic fields can clearly be separated. Our preferred model agrees with previous descrip-
 607 tions of a strong axisymmetric internal field. The model also show a quadrupole-to-dipole
 608 ratio of approximately 0.27, that is very similar to the value reported by Thébault et al.
 609 (2018), though our modeling approach fundamentally differs.

610 To study the time-varying magnetic fields of Mercury, we derive magnetic field resid-
 611 uals from magnetic field measurements and our preferred steady magnetic field model
 612 up to degree and order 3. A time-varying model is derived from magnetic field residu-
 613 als, which are sorted into temporal bins so that each bin contains 8 consecutive orbits
 614 (provided that there are no significant gaps between orbits). For each subset, a spher-
 615 ical harmonic degree 3 internal and spherical harmonic degree 1 external magnetic field
 616 model is computed. The misfit of each subset significantly improves, decreasing from about
 617 26 nT (after the removal of the steady magnetic field) to an average of 15 and as low as
 618 4 nT, depending on the epoch. A covariance analysis indicate a robust separation of the
 619 time-varying external and internal magnetic field coefficients. These individual models
 620 form the time series of the time-varying internal and external field coefficients.

621 We analyze their temporal variability. We adopt the multi-taper method to esti-
 622 mate the spectra of the temporal variability of the internal and external magnetic field,
 623 and to detect mutual coherent signatures in the series. A wavelet method is also applied

624 to identify coherent signatures and their transient behavior. Mercury’s external and in-
625 ternal fields show significant variations related to its orbital motion around the Sun and
626 solar rotation. These variations are coherent and synchronous and indicate the exter-
627 nal field variation induces internal magnetic field within Mercury. The absence of phase
628 lags between the exciting magnetic field variations and their induced responses allows
629 us to place an upper limit on the electrical mantle conductivity of about 1 S/m. Based
630 on the amplitude ratio of exciting external field variation and the internally induced mag-
631 netic field, we estimate Mercury’s core size to be $r_c = 2060 \pm 22$ km. This value is in
632 very good agreement with core size estimates from geodetic observations of Mercury’s
633 gravity field.

634 Some features of this study remain not fully understood, and relate to the low vari-
635 ability of dipole moments during a time interval centered around 2013.2. Likely, this long-
636 term variation of the magnetic dipole moments is related to the absence of coherent vari-
637 ations during this time interval, as seen in Figure 10. The change of MESSENGER’s or-
638 bit geometry could explain the long-term variability of the dipole moments, but not their
639 different amplitudes. Therefore, to what extent this can be explained by the change of
640 MESSENGER’s orbit geometry needs to be understood, and if there is a common cause
641 for these features. The un-even data distribution over the planet’s hemispheres restricts
642 conclusions from our analysis, but this will be overcome by the BepiColombo mission,
643 which will sample Mercury’s magnetic field evenly.

644 **Acknowledgments**

645 The MESSENGER mission was supported by the NASA Discovery Program under con-
646 tracts NAS5-97271 to The Johns Hopkins University Applied Physics Laboratory and
647 NASW-00002 to the Carnegie Institution of Washington. All MESSENGER data used
648 here are publicly available on NASA’s Planetary Data System (PDS) at [http://ppi.pds](http://ppi.pds.nasa.gov)
649 [.nasa.gov](http://ppi.pds.nasa.gov). This research is supported by the French Agence Nationale de la Recherche,
650 project MARMITE, contract 654 ANR-13-BS05-0012, as well as by Centre National des
651 Etudes Spatiales in the context of the BepiColombo MAG experiment. The authors would
652 like to thank Daniel Heyner for stimulating discussions, A. Rösch and H. Schmidtbauer
653 for their help on Waveletcomp. All graphics were produced using opensource software,
654 GMT, gnuplot and R-packages.

655 The authors declare that they have no competing interests.

656 **References**

- 657 Aharonson, O., Zuber, M. T., & Solomon, S. C. (2004). Crustal remanence
 658 in an internally magnetized non-uniform shell: a possible source for Mer-
 659 cury’s magnetic field? *Earth Planet. Sci. Lett.*, *218*. doi: 10.1016/
 660 S0012-821X(03)00682-4
- 661 Anderson, B. J., Acuña, M. H., Korth, H., Purucker, M. E., Johnson, C. L.,
 662 Slavin, J. A., ... McNutt, R. L. (2008). The Structure of Mercury’s Mag-
 663 netic Field from MESSENGER’s First Flyby. *Science*, *321*, 82-85. doi:
 664 10.1126/science.1159081
- 665 Anderson, B. J., Johnson, C. L., & Korth, H. (2013). A magnetic disturbance
 666 index for Mercury’s magnetic field derived from MESSENGER Magnetome-
 667 ter data. *Geochemistry, Geophysics, Geosystems*, *14*(9), 3875-3886. doi:
 668 10.1002/ggge.20242
- 669 Anderson, B. J., Johnson, C. L., Korth, H., Slavin, J. A., Winslow, R. M., Phillips,
 670 R. J., ... Solomon, S. C. (2014). Steady-state field-aligned currents at Mer-
 671 cury. *Geophys. Res. Lett.*, *41*, 7444-7452. doi: 10.1002/2014GL061677
- 672 Anderson, B. J., Johnson, C. L., Korth, H., Winslow, R. M., Borovsky, J. E., Pu-
 673 rucker, M. E., ... McNutt Jr., R. L. (2012). Low-degree structure in Mercury’s
 674 planetary magnetic field. *J. Geophys. Res.*, *117*. doi: 10.1029/2012JE004159
- 675 Bloxham, J., Gubbins, D., & Jackson, A. (1989). Geomagnetic secular variation.
 676 *Philos. Trans. R. Soc. London A*, *329*, 415-502.
- 677 Chapman, S., & Ferraro, V. C. A. (1940). The theory of the first phase of a geomag-
 678 netic storm. *Ter. Mag. and Atm. Elec.*, *45*. doi: 10.1029/TE045i003p00245
- 679 Chapman, S., & Ferraro, V. C. A. (1941). The Geomagnetic Ring-Current: I Its Ra-
 680 dial Stability. *Ter. Mag. and Atm. Elec.*, *46*. doi: 10.1029/TE046i001p00001
- 681 Christensen, U. R. (2006). A deep dynamo generating Mercury’s magnetic field. *Na-*
 682 *ture*, *444*. doi: 10.1038/nature05342
- 683 Christensen, U. R., Aubert, J., & Hulot, G. (2010). Conditions for Earth-like geody-
 684 namo models. *Earth Planet. Sci. Lett.*, *296*(3-4), 487-496. doi: {10.1016/j.epsl
 685 .2010.06.009}
- 686 Connerney, J. E. P., Kotsiaros, S., Oliverson, R. J., Espley, J. R., Joergensen, J. L.,
 687 Joergensen, P. S., ... Levin, S. M. (2018). A New Model of Jupiter’s Mag-
 688 netic Field From JUNO’s First Nine Orbits. *Geophys. Res. Lett.*, *45*. doi:

- 689 10.1002/2018GL077312
- 690 de Boor, C. (1978). *A practical guide to splines*. Springer-Verlag, New York.
- 691 Finlay, C. C., Lesur, V., Thébault, E., Vervelidou, F., Morschhauser, A., &
692 Shore, R. (2016). Challenges Handling Magnetospheric and Ionospheric
693 Signals in Internal Geomagnetic Field Modelling. *Space Sci. Rev.* doi:
694 10.1007/s11214-016-0285-9
- 695 Ghil, M., Allen, M. R., Dettinger, M. D., Ide, K., Kondrashov, D., Mann, M. E., ...
696 Yiou, P. (2002). Advanced spectral methods for climatic time series. *Rev.*
697 *Geophys.*, *40*, 1-41.
- 698 Glassmeier, K.-H. (2000). Currents in Mercury's Magnetosphere. *Geophys. Mono.*
699 *Series*, *118*. doi: 10.1029/GM118p0371
- 700 Glassmeier, K.-H., Auster, H.-U., & Motschmann, U. (2007). A feedback dynamo
701 generating Mercury's magnetic field. *Geophys. Res. Lett.*, *34*. doi: 10.1029/
702 2007GL031662
- 703 Gómez-Pérez, N., Heimpel, M., & Wicht, J. (2010). Effects of a radially varying
704 electrical conductivity on 3D numerical dynamos. *Phys. Earth Planet. Int.*,
705 *181*. doi: 10.1016/j.pepi.2010.03.006
- 706 Gómez-Pérez, N., & Solomon, S. C. (2010). Mercury's weak magnetic field:
707 A result of magnetospheric feedback? *Geophys. Res. Lett.*, *37*. doi:
708 10.1029/2010GL044533
- 709 Grinsted, A., Moore, J. C., & Jevrejeva, S. (2004). Application of the cross wavelet
710 transform and wavelet coherence to geophysical time series. *Nonlin. Proc. Geo-*
711 *phy*, *11*, 561-566.
- 712 Grosser, J., Glassmeier, K.-H., & Stadelmann, A. (2004). Induced magnetic field ef-
713 fects at planet Mercury. *Planet. Spa. Sci.*, *52*. doi: 10.1016/j.pss.2004.08.005
- 714 Gubbins, D. (1983). Geomagnetic field analysis – i. stochastic inversion. *Geophys. J.*
715 *R. Astr. Soc.*, *73*, 641-652.
- 716 Hauck, S. A., Margot, J.-L., Solomon, S. C., Phillips, R. J., Johnson, C. L.,
717 Lemoine, F. G., ... Zuber, M. T. (2013). The curious case of Mercury's inter-
718 nal structure. *J. Geophys. Res.*, *118*(6), 1204-1220. doi: 10.1002/jgre.20091
- 719 Heyner, D., Nabert, C., Liebert, E., & Glassmeier, K.-H. (2016). Concerning
720 reconnection-induction balance at the magnetopause of Mercury. *J. Geophys.*
721 *Res. (Spa. Phys.)*, *121*. doi: 10.1002/2015JA021484

- 722 Heyner, D., Wicht, J., Gómez-Pérez, N., Schmitt, D., Auster, H.-U., & Glass-
 723 meier, K.-H. (2011). Evidence from Numerical Experiments for a Feed-
 724 back Dynamo Generating Mercury’s Magnetic Field. *Science*, *334*. doi:
 725 10.1126/science.1207290
- 726 Holme, R., & Bloxham, J. (1996). The magnetic fields of Uranus and Neptune:
 727 Methods and models. *J. Geophys. Res.*, *101*, 2177-2200.
- 728 Hood, L., & Schubert, G. (1979). Inhibition of solar wind impingement on Mer-
 729 cury by planetary induction currents. *J. Geophys. Res.*, *84*. doi: 10.1029/
 730 JA084iA06p02641
- 731 Jackson, D. D. (1979). The use of a priori data to resolve nonuniqueness in linear in-
 732 version. *Geophys. J. R. Astr. Soc.*, *57*, 137-157.
- 733 Johnson, C. L., Philpott, L. C., Anderson, B. J., Korth, H., Hauck, S. A., Heyner,
 734 D., . . . Solomon, S. C. (2016). MESSENGER observations of induced magnetic
 735 fields in Mercury’s core. *Geophys. Res. Lett.*, *43*. doi: 10.1002/2015GL067370
- 736 Johnson, C. L., Purucker, M. E., Korth, H., Anderson, B. J., Winslow, R. M.,
 737 Al Asad, M. M. H., . . . Solomon, S. C. (2012). MESSENGER observa-
 738 tions of Mercury’s magnetic field structure. *J. Geophys. Res.*, *117*. doi:
 739 10.1029/2012JE004217
- 740 Korth, H., Johnson, C. L., Philpott, L., Tsyganenko, N. A., & Anderson, B. J.
 741 (2017). A Dynamic Model of Mercury’s Magnetospheric Magnetic Field. *Geo-*
 742 *phys. Res. Lett.*, *44*, 10. doi: 10.1002/2017GL074699
- 743 Korth, H., Tsyganenko, N. A., Johnson, C. L., Philpott, L. C., Anderson, B. J., Al
 744 Asad, M. M., . . . McNutt, R. L. (2015). Modular model for Mercury’s mag-
 745 netospheric magnetic field confined within the average observed magnetopause.
 746 *J. Geophys. Res.*, *120*, 4503-4518. doi: 10.1002/2015JA021022
- 747 Lall, U., & Mann, M. (1995). The Great Salt Lake: A Barometer of Low-Frequency
 748 Climatic Variability. *Water Res. Res.*, *31*. doi: 10.1029/95WR01950
- 749 Langel, R. A. (1987). Geomagnetism, Vol. 1, Jacobs, J. A., Ed. In (p. 249-512). Aca-
 750 demic Press.
- 751 Langlais, B., Purucker, M. E., & Mandea, M. (2004). Crustal magnetic field of Mars.
 752 *J. Geophys. Res.*, *109*. doi: 10.1029/2003JE002048
- 753 Lesur, V., Rother, M., Wardinski, I., Schachtschneider, R., Hamoudi, M., & Cham-
 754 bodut, A. (2015). Parent magnetic field models for the IGRF-12 GFZ-

- 755 candidates. *Earth Planets Space*, 67. doi: 10.1186/s40623-015-0239-6
- 756 Levenberg, K. (1944). A Method for the Solution of Certain Non-Linear Problems in
757 Least Squares. *Quart. Appl. Math.*, 2, 164-168.
- 758 Lowes, F. J. (1966). Mean-square values on sphere of spherical harmonic vector
759 fields. *J. geophys. Res.*, 71, 2179.
- 760 Mann, M. E., & Lees, J. M. (1996). Robust estimation of background noise and sig-
761 nal detection in climatic time series. *Climate Change*, 33, 409-445.
- 762 Mann, M. E., & Park, J. (1993). Spatial correlations of interdecadal vari-
763 ation in global surface temperatures. *Geophys. Res. Lett.*, 20. doi:
764 10.1029/93GL00752
- 765 Margot, J. L., Peale, S. J., Jurgens, R. F., Slade, M. A., & Holin, I. V. (2007). Large
766 Longitude Libration of Mercury Reveals a Molten Core. *Science*, 316. doi: 10
767 .1126/science.1140514
- 768 Mauersberger, P. (1956). Das Mittel der Energiedichte des geomagnetischen Haupt-
769 feldes an der Erdoberfläche und seine säkulare Änderung. *Gerlands Beiträge
770 zur Geophysik*, 65, 207-215.
- 771 Ness, N. F., Behannon, K. W., Lepping, R. P., Whang, Y. C., & Schatten, K. H.
772 (1974a). Magnetic Field Observations near Mercury: Preliminary Results from
773 Mariner 10. *Science*, 185, 151-160.
- 774 Ness, N. F., Behannon, K. W., Lepping, R. P., Whang, Y. C., & Schatten, K. H.
775 (1974b). Observations at Mercury encounter by the plasma science experiment
776 on Mariner 10. *Science*, 185, 159-170.
- 777 Oliveira, J. S., Langlais, B., Pais, M. A., & Amit, H. (2015). A modified Equiv-
778 alent Source Dipole method to model partially distributed magnetic field
779 measurements, with application to Mercury. *J. Geophys. Res.*, 120. doi:
780 10.1002/2014JE004734
- 781 Olsen, N. (1999). Induction studies with satellite data. *Surveys in Geophysics*, 20,
782 309-340. doi: 10.1023/A:1006611303582
- 783 Park, J., Lindberg, C. R., & Vernon, F. L. (1987). Multitaper spectral analysis of
784 high-frequency seismograms. *J. Geophys. Res.*, 92, 12675-12684.
- 785 Parkinson, W. D., & Hutton, V. R. S. (1989). The electrical conductivity of the
786 Earth. *Geomatik*, 3, 261-321.
- 787 Percival, D. B., & Walden, A. T. (1993). *Spectral analysis for physical applications*.

- 788 *multitaper and conventional univariate techniques*. Cambridge, UK: Cambridge
789 University Press.
- 790 Ridley, V. A., & Holme, R. (2016). Modeling the Jovian magnetic field and its sec-
791 ular variation using all available magnetic field observations. *J. Geophys. Res.*,
792 *121*. doi: 10.1002/2015JE004951
- 793 Rikitake, T. (1966). *Electromagnetism and the Earth's Interior*. Elsevier Publishing
794 Company, Amsterdam, London, New York.
- 795 Rivoldini, A., & Van Hoolst, T. (2013). The interior structure of Mercury con-
796 strained by the low-degree gravity field and the rotation of Mercury. *Earth*
797 *Planet. Sci. Lett.*, *377*. doi: 10.1016/j.epsl.2013.07.021
- 798 Rivoldini, A., Van Hoolst, T., & Verhoeven, O. (2009). The interior structure of
799 Mercury and its core sulfur content. *Icarus*, *201*. doi: {10.1016/j.icarus.2008
800 .12.020}
- 801 Slavin, J. A., Owen, J. C. J., Connerney, J. E. P., & Christon, S. P. (1997). Mariner
802 10 observations of field-aligned currents at Mercury. *Planetary and Space Sci-*
803 *ence*, *45*, 133-141. doi: 10.1016/S0032-0633(96)00104-3
- 804 Solomon, S. C., McNutt, R. L., Gold, R. E., & Domingue, D. L. (2007). MESSEN-
805 GER Mission Overview. *Space Sci. Rev.*, *131*. doi: 10.1007/s11214-007-9247-6
- 806 Stevenson, D. J. (1987). Mercury's magnetic field - A thermoelectric dynamo? *Earth*
807 *Planet. Sci. Lett.*, *82*. doi: 10.1016/0012-821X(87)90111-7
- 808 Suess, S. T., & Goldstein, B. E. (1979). Compression of the Hermean magnetosphere
809 by the solar wind. *J. Geophys. Res.*, *84*. doi: 10.1029/JA084iA07p03306
- 810 Tarantola, A. (1987). *Inverse problem theory. Methods for data fitting and model pa-*
811 *rameter estimation*. Amsterdam: Elsevier, 1987.
- 812 Tarits, P., & Grammatica, N. (2000, December). Electromagnetic induction effects
813 by the solar quiet magnetic field at satellite altitude. *Geophys. Res. Lett.*, *27*,
814 4009-4012. doi: 10.1029/1999GL011249
- 815 Thébaud, E., Finlay, C. C., Beggan, C., Alken, P., Aubert, J., Barrois, O., ...
816 Zvereva, T. (2015). International geomagnetic reference field: the twelfth
817 generation. *Earth Planets Space*, *67*. doi: 10.1186/s40623-015-0228-9
- 818 Thébaud, E., Langlais, B., Oliveira, J. S., Amit, H., & Leclercq, L. (2018). A time-
819 averaged regional model of the Hermean magnetic field. *Phys. Earth Planet.*
820 *Int.*, *276*. doi: 10.1016/j.pepi.2017.07.001

- 821 Thébault, E., Schott, J. J., & Manda, M. (2006). Revised Spherical Cap Harmonic
822 Analysis (R-SCHA): Validation and Properties. *J. Geophys. Res.*, *111*. doi: 10
823 .1029/2005JB003836
- 824 Thébault, E., Vervelidou, F., Lesur, V., & Hamoudi, M. (2012). The shortcomings
825 of the along-track satellite filtering in planetary magnetism. *Geophys. J. Int.*,
826 *188*, 891-907. doi: 10.1111/j.1365-246X.2011.05281.x
- 827 Thomson, D. J. (1982). Spectrum estimation and harmonic analysis. *IEEE Proc.*,
828 *70*, 1055–1096.
- 829 Torrence, C., & Webster, P. J. (1999). Interdecadal Changes in the ENSO-Monsoon
830 System. *J. Clim.*, *12*. doi: 10.1175/1520-0442(1999)012<2679:ICITEM>2.0.CO;
831 2
- 832 Tsyganenko, N. A., & Sitnov, M. I. (2005). Modeling the dynamics of the inner
833 magnetosphere during strong geomagnetic storms. *J. Geophys. Res.*, *110*. doi:
834 10.1029/2004JA010798
- 835 Uno, H., Johnson, C. L., Anderson, B. J., Korth, H., & Solomon, S. C. (2009). Mod-
836 eling Mercury’s internal magnetic field with smooth inversions. *Earth Planet.*
837 *Sci. Lett.*, *285*. doi: 10.1016/j.epsl.2009.02.032
- 838 Verhoeven, O., Tarits, P., Vacher, P., Rivoldini, A., & Van Hoolst, T. (2009).
839 Composition and formation of Mercury: Constraints from future elec-
840 trical conductivity measurements. *Planet. Spa. Sci.*, *57*, 296-305. doi:
841 10.1016/j.pss.2008.11.015
- 842 Vernon, F. L., Fletcher, J., Carroll, L., Chave, A., & Sembera, E. (1991). Coherence
843 of seismic body waves from local events as measured by a small-aperture array.
844 *J. Geophys. Res.*, *96*. doi: 10.1029/91JB00193
- 845 Winslow, R. M., Anderson, B. J., Johnson, C. L., Slavin, J. A., Korth, H., Purucker,
846 M. E., ... Solomon, S. C. (2013). Mercury’s magnetopause and bow shock
847 from MESSENGER Magnetometer observations. *J. Geophys. Res.*, *118*. doi:
848 10.1002/jgra.50237
- 849 Zhang, Z., & Pommier, A. (2017). Electrical Investigation of Metal-Olivine Systems
850 and Application to the Deep Interior of Mercury. *J. Geophys. Res.*, *122*. doi:
851 10.1002/2017JE005390

Table 1. Inversion parameters and diagnostics

scheme	MBF_alt	MBF_mag	MBF_a-n
number of vector triplets	3682144	3333520	1413988
rms misfit (nT)	31.14	29.68	26.22
λ_s	4.0×10^6	4.0×10^4	4.0×10^2

Table 2. Comparison of previous and steady magnetic field models of this study based on different modeling techniques and data selection schemes.

coefficients	MBF_alt	MBF_mag	MBF_a-n	Anderson et al. 2012	Thebault et al. 2018
g_1^0	-197.1	-200.0	-215.8	-190.0	-213.6
g_1^1	-2.9	1.1	0.2	–	0.9
h_1^1	1.5	0.8	2.7	–	1.5
g_2^0	-83.2	-80.9	-57.0	-74.6	-57.7
g_2^1	3.4	-1.5	1.0	–	–
h_2^1	0.0	0.2	-1.4	–	–
g_2^2	-1.4	-0.8	-7.0	–	–
h_2^2	0.4	-0.2	-3.3	–	–
g_3^0	-15.7	-16.3	-36.7	-22.0	-35.8
g_3^1	1.8	4.1	2.9	–	–
g_3^1	0.3	0.4	0.8	–	–
g_3^2	-1.5	-1.5	9.2	–	–
h_3^2	0.9	1.3	2.6	–	–
g_3^3	-1.4	-1.5	-2.5	–	–
h_3^3	0.3	0.2	0.1	–	–
q_1^0	-39.7	-39.2	-23.2	–	-39.7
q_1^1	0.6	0.2	-0.2	–	0.7
s_1^1	1.3	1.5	0.4	–	-0.1

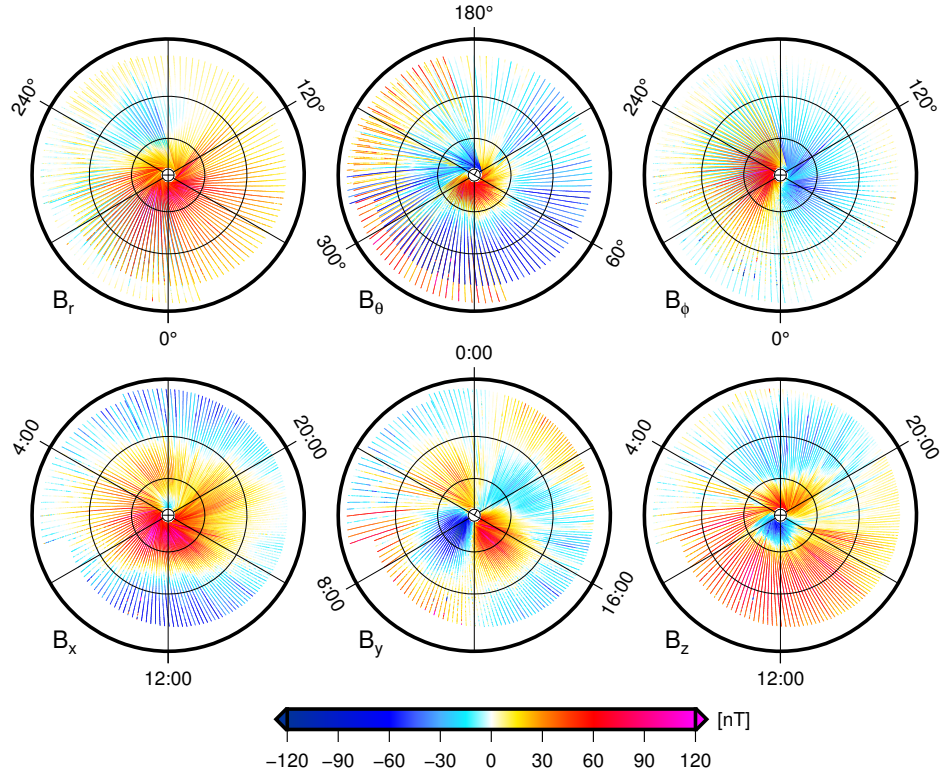


Figure 1. North polar view of residuals, after subtraction of the steady field, of the (top) δB_r , δB_θ and δB_ϕ field components in the MBF coordinate system, and (bottom) δB_x , δB_y and δB_z field components in the MSO coordinate system, from left to right. Maps in the bottom panel are organized with respect to local times. All maps show residuals for the period from 2011.48 to 2011.72, i.e., one Hermean year (88 terrestrial days). Black circles are spaced 30° in latitude.

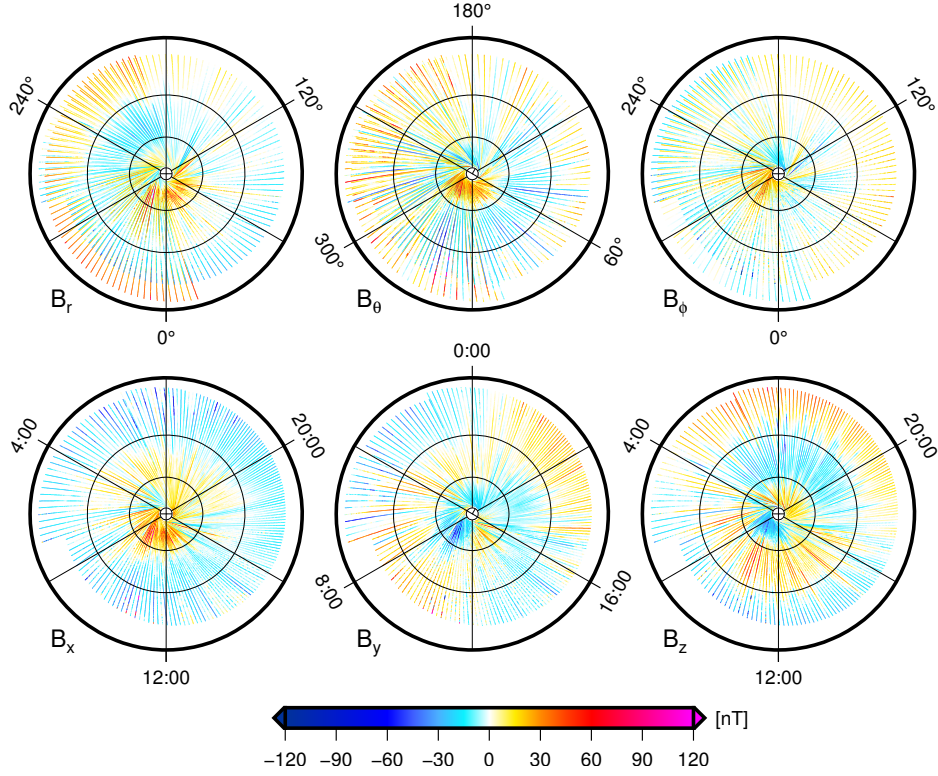


Figure 2. North polar view of residuals, after subtraction of the time-varying field. The same arrangement as in Figure 1 is applied.

Figure 3. Time series of the Gauss coefficients derived from the residual field data in the MBF coordinate system. Axial terms are shown in the top panel and equatorial terms in the bottom panel, respectively. The colors of individual curves are defined in the figure legends.

Figure 4. The temporal evolution of MESSENGER’s periapsis latitude.

Figure 5. Time series of the internal and external magnetic dipole moments, $\delta M_{\text{int}}(t)$ and $M_{\text{ext}}(t)$, respectively.

Figure 6. Comparison of the time varying external magnetic dipole moment with Mercury’s heliocentric distance (right axis, in astronomical units [au]). The bottom panels show the location of MESSENGER at different epochs, each when the orbiter was in a noon-midnight plane. Color depicts the altitude of the spacecraft, with the lowermost point shown as a star. The panels 1 and 2, 3 and 4, and 5 and 6 are separated by a constant interval of 54 (terrestrial) days.

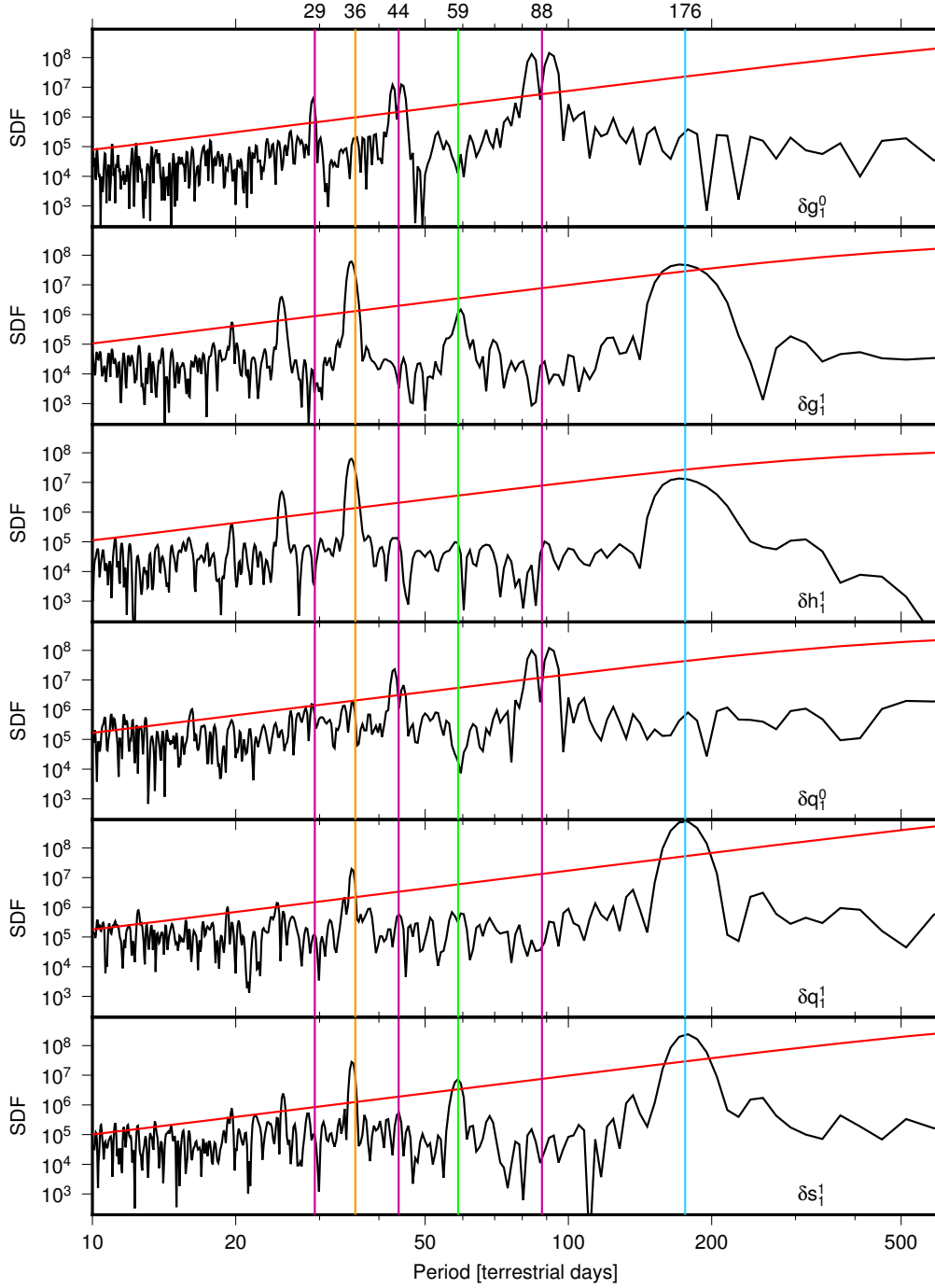


Figure 7. Power spectra of the first three internal and external field Gauss coefficients as labeled in the individual plots. Dark magenta vertical bars mark Mercury’s orbital period around the Sun and its harmonics (88, 44 days and 29 days), respectively. Orange bars identify the synodic rotation period of the Sun (36 days), light-green bar marks Mercury’s rotation period (59 days), and the light-blue bars mark the 176-days period, one solar day on Mercury. The red line displays 95%-level of significance, corresponding to the pure line test described in the text.

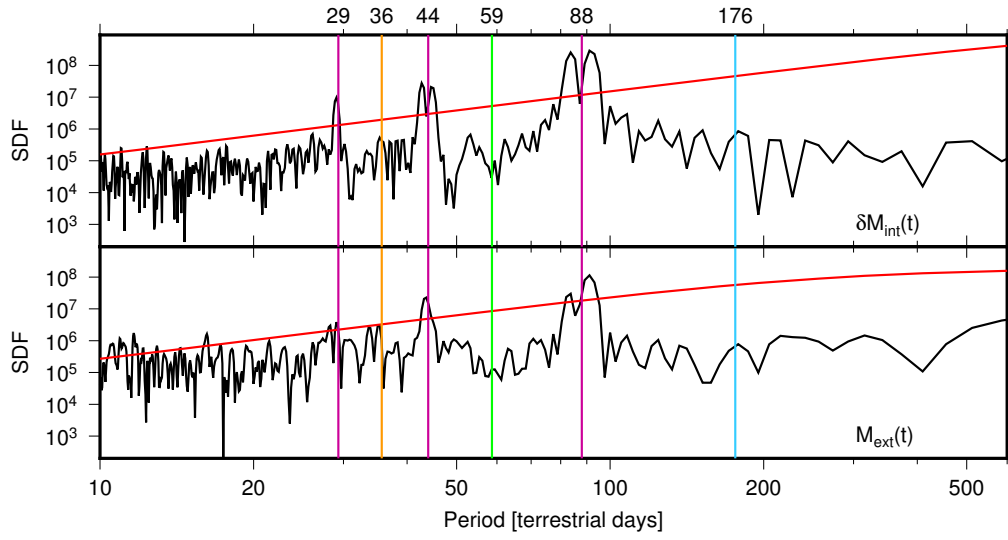


Figure 8. Power spectra of the internal and external varying dipole moments. The same line-style is applied as in Figure 7.

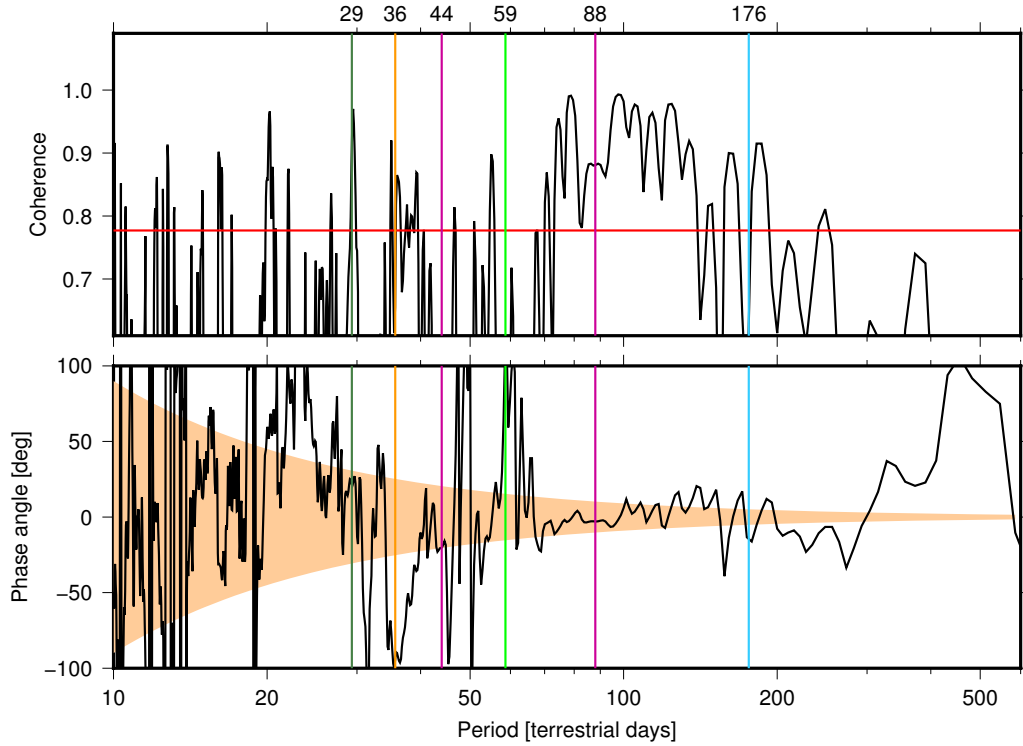


Figure 9. The coherence (top) and phase (bottom) spectra of $\delta M_{\text{int}}(t)$ and $M_{\text{ext}}(t)$ time series. The red line in the coherence spectrum marks 95% level of significance, where the colored area in the phase spectrum marks uncertainties of a 0 degree phase determined by the temporal resolution of the series. In this range phase angles are indistinguishable from zero. A positive phase angle relates to a leading of $\delta M_{\text{int}}(t)$ before $M_{\text{ext}}(t)$, whereas a negative phase angle corresponds to a trailing of $\delta M_{\text{int}}(t)$. The light colored region displays the range of un-resolved phase angles. Colors of vertical bars to identify prominent periods are the same as in Figure 8.

Figure 10. The wavelet coherence of $\delta M_{\text{int}}(t)$ and $M_{\text{ext}}(t)$. Dark red areas encircled by a gray line indicate significant coherent signal (significance level $> 95\%$).

Figure A.1. Covariance matrix of the preferred model MBF_a-n. The numbering of the coefficients is $g_1^0 = 1$; $g_1^1 = 2$; $h_1^1 = 3$; $g_2^0 = 4$; $g_2^1 = 5$ and so on. External coefficients are 16-18.

A Covariance analysis

We study the robustness of the constrained inversion by analysing the covariance matrix that is given by

$$\mathbf{C} = \hat{\sigma}^2(\mathbf{A}^\top \mathbf{C}_e^{-1} \mathbf{A} + \mathbf{C}_m)^{-1} \quad (\text{A.1})$$

where $\hat{\sigma}^2$ is the misfit of the model. The covariance matrix quantifies the uncertainties in the model estimates due to linear dependence between model parameters. Ideally, one would expect this matrix to be purely diagonal, but in fact some non-diagonal elements are not zero, which indicates a dependency between coefficients of the same degree but different order.

In Figure A.1 covariance matrix of our preferred steady field models in the MBF coordinate system is shown. The plot shows largely positive diagonal elements, which correspond to the covariance between identical coefficients, i.e. $\mathbf{C}(2, 2)$ etc. We also observe large values of covariances between different coefficients. Most noticeable are large correlation between the first six internal coefficients g_1^0, \dots, h_2^1 . Similar structures are found for the covariances between coefficients of the first and third spherical harmonic degrees, and between degree 1 and 4, but with smaller covariance values.

We tend to assume that large values of the covariance between different internal coefficients could be caused by the particular orbital configuration of the MESSENGER mission, with no magnetic field measurement over Mercury's southern hemisphere. Estimations of spherical harmonic coefficients with even spherical harmonic degrees may be prone to such data distribution. No significant covariance between internal and external coefficients (coefficient numbers 16, 17 and 18) is found, which may indicate a good separation between these field contributions in our modeling.

Figure A.2 shows maps of covariance matrices for different epochs during the mission interval. The covariance structure of these maps varies with time, as it can be deduced from the different patterns in the maps, but values of the covariance are largely

Figure A.2. Covariance matrices for different epochs of time varying magnetic field model derived from residuals between MBF_a-n and MESSENGER measurements. Top panel epochs around 2011.7, middle panel around 2013.2 and bottom panel around 2015.2.

877 reduced. Again, there seems to be no indication of significant covariance between exter-
878 nal and internal field coefficients.

879 B Spectral and coherence analysis

880 The spectral analysis of series of the Gauss coefficients and the external and inter-
881 nal dipole moments is conducted by using the multi-taper method (MTM). The MTM
882 was originally developed by Thomson (1982) and proved to provide robust spectral es-
883 timates of geophysical and climatic time series (Park et al., 1987; Percival & Walden,
884 1993; Ghil et al., 2002). Furthermore, it performs particularly well for short time series
885 (Park et al., 1987; Mann & Lees, 1996), which may be applicable for this study. The method
886 provides a spectral estimate with an optimal trade-off between spectral resolution and
887 residual variance, where the trade-off is determined by the choice of the bandwidth of
888 spectral resolution controlled by an integer p . The number of tapers M is then defined
889 accordingly.

890 We tested several MTM-parameter sets $\{p, M\}$, and the sets $\{p, M\} = \{1, 1\}, \{2, 3\}$
891 show minimal variances of the residual signal between time series and their reconstruc-
892 tions from the spectrum. In order to have highly resolved spectra we apply $p = 1, M =$
893 1 in this study. Moreover, we consider the period range between 5 and 500 days as ro-
894 bustly resolved. The limit towards longer periods is set by the total length of time se-
895 ries, which is about 1492 days long and represents the duration of the mission around
896 Mercury. This implicitly requires that periods should occur at least three times. At the
897 short end, shorter periods than 5 days may not be resolved, because of the orbital sam-
898 pling and the subsequent spline interpolation.

899 To estimate the coherence of two individual time series, we apply two different meth-
900 ods. First, we derive the coherence across two time series by following closely Vernon et
901 al. (1991), Mann and Park (1993), and Lall and Mann (1995): the coherence of two sig-
902 nals is determined by the individual spectral density functions (SDF) of the series us-
903 ing the multi-taper method. We refer to this as MTM-coherence. Secondly, we use a wavelet

904 based analysis of the series that were developed by Torrence and Webster (1999) and Grin-
905 sted et al. (2004). The wavelet-coherence provide a localized correlation coefficient in the
906 time-frequency space (Grinsted et al., 2004), whereas the MTM-coherence gives a global
907 (averaged) estimate. The wavelet-coherence is sensitive to quasi-periodic variations.

908 A coherence value of unity indicates complete dependence of one signal on another,
909 whereas a coherence value of zero refers to no dependence of one signal on another. Two
910 signals can only be coherent at the same frequency, and may have a phase that varies
911 between ± 180 degree. Both methods provide estimates of phases between coherent sig-
912 nals.

913 In this study, we apply a pure line test as given by Mann and Lees (1996) to ver-
914 ify the significance of spectral and coherent features against the null hypothesis of a red
915 noise background. Contrary to a white noise process, with no correlation between sin-
916 gle observations, red noise process include some long term correlations, such as a linear
917 trend. The spectrum of a red noise process is estimated by the spectrum of a first or-
918 der auto-regressive process. This pure line test is used to assess the robustness of our
919 results in the next section.